scientific reports

Check for updates

OPEN

Computational assessment of blood lipid influence on hemodynamics in human retinal vessels

Yu Ding[1,2], Zhengxuan Jiang[1], Jiang Jiang[2], Guoke Yang[2], Yinglong Li[2] & Liming Tao[1]✉

The study of retinal hemodynamics is pivotal for understanding both physiological and pathological conditions affecting the eye. Microcirculation in the retina exhibits unique rheological properties and flow dynamics compared to larger vessels. This computational study investigates the possible impact of elevated blood lipids on retinal vascular flow characteristics, focusing on viscosity increases and potential blockage effects. We utilized computational fluid dynamics to solve the incompressible Navier-Stokes equations for an image-based retinal vessel network under healthy conditions. Our findings reveal that arterial vessels have a higher average mainstream flow velocity than venous vessels, however, the latter experience higher wall shear stress (WSS) in those fine branch vessels, which are far away from the optical disc. Notably, vessels with more branches in the venous network are subjected to greater WSS. Then, we simulated the effect of elevated blood lipids by increasing venous viscosity by about 10-20%, which led to a proportional rise in WSS. Furthermore, we explored the potential blockage that may caused by elevated blood lipids, leading to localized increases in velocity and WSS. This study provides insights into the hemodynamic alterations induced by hyperlipidemia, highlighting the importance of considering systemic health parameters in ocular disease research and treatment.

Keywords Blood lipids, Retinal vessels, Computational analysis

The process of vision initiates in the retina, where intricate neural circuits extract prominent features of the surrounding environment from the incoming light through our eyes[1,2]. The retina is composed of a network of neurons and supporting cells that require a constant and efficient blood supply in order to function optimally. The retinal blood vessel network plays a crucial role in maintaining homeostasis by facilitating the delivery of nutrients and removal of waste, which are essential for the survival of photoreceptors and other retinal neurons[3]. Disruption of blood flow within the microvascular network can lead to a variety of ocular diseases, including diabetic retinopathy[4], retinal vein occlusion[5], and age-related macular degeneration[6]. These conditions have the potential to cause severe visual impairment or even blindness. Therefore, comprehending the underlying hemodynamics of retinal microcirculation is crucial for unraveling the pathophysiology of these disorders.

One of the significant factors influencing retinal blood flow dynamics is the presence of elevated blood lipids, a condition prevalent in modern society due to increasing obesity rates and dietary patterns high in saturated fats. The presence of hyperlipidemia can impact the rheological characteristics of blood[7], including viscosity and flow dynamics, thereby leading to alterations in perfusion parameters within the retinal vascular network. Elevated lipid levels have been associated with increased vascular resistance and impaired endothelial function, which may contribute to inadequate blood supply and subsequent retinal ischemia[8,9], particularly under conditions of heightened metabolic demand. Despite these implications, the specific quantitative effects of hyperlipidemia on retinal blood flow dynamics remain inadequately explored in the literature, especially based on computational analysis.

To address this research gap, this study employs computational fluid dynamics (CFD), which allows for the detailed modeling of complex fluid interactions within the retinal blood vessel network[10–13]. By simulating blood flow under conditions of elevated blood lipids, we seek to elucidate the hemodynamic alterations that occur within this critical vascular area. CFD offers a unique advantage in visualizing flow patterns, wall shear stresses,

[1]Department of Ophthalmology, The Second Affiliated Hospital of Anhui Medical University, Hefei 230601, China. [2]Department of Ophthalmology, The First People's Hospital of Hefei, The Third Affiliated Hospital of Anhui Medical University, Hefei 230032, China. ✉email: taoliming@ahmu.edu.cn

and velocity distributions[10,14–16], enabling quantitative analysis of how increased lipid levels may impact retinal hemodynamics. Insights gained from this computational exploration can inform researchers and clinicians about the critical interplay between elevated blood lipids and retinal blood flow, potentially guiding clinical interventions to prevent or mitigate hyperlipidemia-associated retinal diseases.

As the field of ocular medicine and computational modeling continues to evolve, it is paramount to explore how systemic health conditions such as hyperlipidemia can influence retinal hemodynamics. Understanding these relationships is crucial for developing therapeutic strategies aimed at managing lipid-induced retinal dysfunction and preserving vision. This investigation not only provides a preliminary understanding of retinal hemodynamics but also highlights the importance of incorporating systemic health parameters in studies focused on ocular disease prevention and treatment.

Results

In this section, we present computational results in various scenarios. Firstly, we conduct a computational analysis of hemodynamics in the retinal arteries and veins, showcasing the distributions of pressure, velocity, and wall shear stress. Secondly, we attempt to investigate the impact of viscosity resulting from elevated blood lipids and perform quantitative analyses. Finally, the potential effects of blockage caused by elevated blood lipid levels are estimated, with particular emphasis on the wall shear stress. This analysis is favourable for understanding the mechanical mechanisms of retinal vein occlusion.

Computational analysis of hemodynamics in the retinal vessels

The analysis begins with an examination of the distributions of velocity and pressure. Figure 1 shows the distributions of static pressure and velocity magnitudes using contour plots in veins and arteries. In the case of veins, as depicted in Fig. 1a, the region with a relatively narrow central blood vessel exhibits a peak velocity of approximately 9 cm/s with a mean velocity of about 5.6 cm/s. The observed value slightly exceeds the prediction reported by Malek et al.[11], potentially attributed to a higher number of modeled Inlets in the current venous tree, resulting in augmented flow rates. Basically, the blood flow velocity increases as the distance from the optic disc decreases. The blood flow exits the venous tree through the mainstream vein, and at the outlet, the peak velocity measures approximately 7 cm/s. In Fig. 1b, the highest pressure drop occurs between the Inlet In6 and Outlet, amounting to approximately 9.9 mmHg. In the case of arteries, the maximum velocity achieved at the central vessels is approximately 11 cm/s, which is in agreement with the finding (11 cm/s) of Malek et al.[11], as well as the clinical data of Medfvil et al. (12.6 ± 2.6 cm/s)[17] and Caca et al.[18] (11.25 ± 2.38 cm/s), as shown in Fig. 1c. The

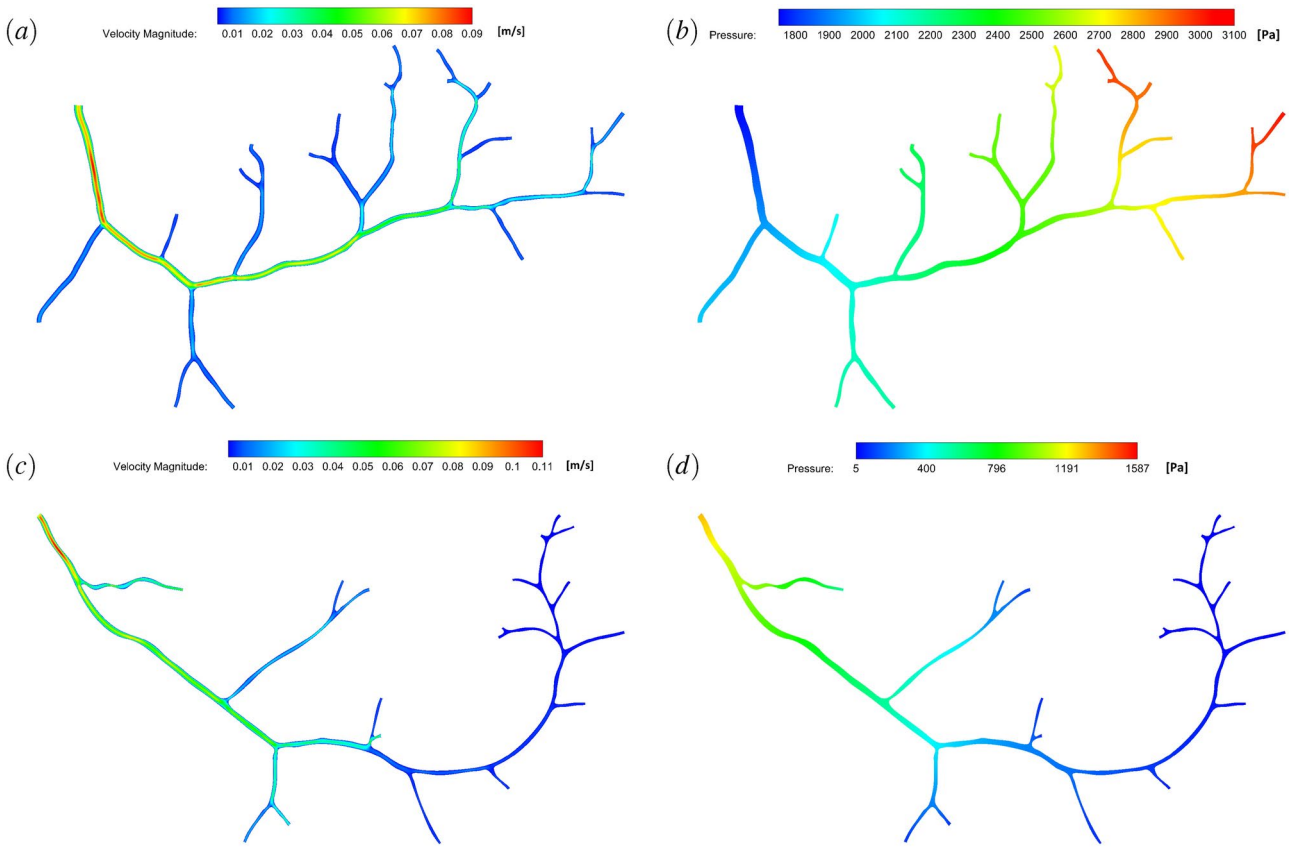

Fig. 1. The distributions of (**a**) velocity magnitude and (**b**) static pressure in the retinal vein network. The distributions of (**c**) velocity magnitude and (**d**) static pressure in the retinal artery network.

maximum pressure drop occurs between the Inlet and Outlet O10/O11, measuring approximately 11 mmHg, which is reasonably consistent with the value reported by Liu et al.[19] for a human retinal circulation. The blood flow decreases rapidly as it moves away from the optic disc region, which allows sufficient time in the arterioles for exchanges with tissue cells in these fine branch vessels due to the slow flow rate.

Wall shear stress (WSS)[20] is crucial in retinal vessels as it influences endothelial cell function, affecting blood flow dynamics and potentially contributing to vascular health and the pathophysiology of retinal diseases such as diabetic retinopathy and retinal vein occlusion. WSS is defined as the frictional force exerted by flowing blood on the endothelial surface of the blood vessel. Mathematically, wall shear stress (τ_{shear}) can be represented by the equation:

$$\tau_{\mathrm{shear}} = \mu \frac{dv_h}{dr}, \tag{1}$$

where v_h is the velocity along the vessel, and r represents the normal distance from the wall. In this study, a macroscopic viscosity value accounting for the Fahraeus-Lindqvist effect is utilized for each segment[12]. It should be noted that, in practical scenarios, the viscosity within the cross-section of the microvessel is inevitably non-uniform due to the lower concentration of red blood cells near the vessel walls. Incorporating this factor into the evaluation of wall shear stress (WSS) remains a significant challenge and has not yet been achieved in the realm of retinal vessels to date. Usually, the magnitude of WSS is influenced by the dynamics of blood flow and varies depending on factors such as vessel shape and curvature. For instance, the changes in WSS levels are positively associated with the development of atherosclerotic plaques, indicating the pivotal role played by WSS in maintaining vascular health.

Figure 2 presents the distributions of WSS magnitude in the retinal venous and artery trees. Comparing Fig. 2a, b, it is found that the arterial mainstream vessel experiences greater WSS compared to the venous mainstream vessel, due to the higher velocity of blood flow as aforementioned. The distribution of WSS is highly nonuniform, primarily influenced by the diameter of the blood vessel and the flow rate, regardless of whether it is in veins or arteries. In a given blood vessel, smaller diameters usually correspond to higher values of WSS. Moreover, the magnitudes of WSS in both the venous and arterial trees are found to be below 10 Pa, which aligns with previous findings[12]. In the case of veins, almost all venous branch vessels experience a certain degree of WSS. A noteworthy observation is that branch vessels with a higher number of bifurcations tend to experience elevated levels of WSS, such as the S22 segment. This is primarily due to the higher blood flow in these vessels. In the case of arteries, the vessels in close proximity to the optic disc region experience significantly higher levels of WSS, whereas those branching further away from this region encounter WSS which is nearly negligible

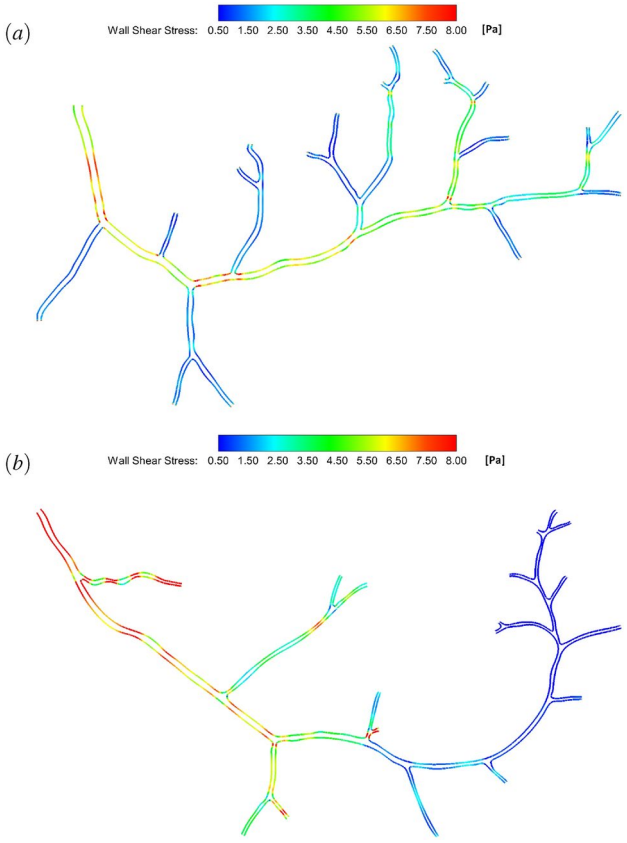

Fig. 2. The distributions of wall shear stress magnitude in the retinal (**a**) venous and (**b**) artery trees.

(e.g. segments S17-S35). This is mainly attributed to the slow flow rate in these vessels, as depicted in Fig. 1c. Additionally, the study of venous vessels from a mechanical perspective is of particular interest due to their structural characteristics. Venous vessels, especially the finer branches, have a reduced capacity to withstand the effects of WSS. This vulnerability can make them more susceptible to damage from the mechanical forces exerted by the blood flow. Therefore, the subsequent discussion will primarily focus on the venous trees.

The effects of blood viscosity

As we know, elevated lipids can increase blood viscosity by causing red blood cell aggregation and altering the plasma composition, making the blood thicker and more resistant to flow. Here, we study the flow with enhanced viscosity to investigate the possible influence on flow characteristics caused by evaluated lipids. Considering that the WSS in the vein network, especially the fine branch vessels, is more significant, only the flow in the vein network is examined. The increase in blood viscosity resulting from high cholesterol is not typically quantified by a simple multiplier due to its dependence on various individual factors. Here, we assumed that individuals with significantly elevated lipid levels may experience about 10–20% rise in blood viscosity compared to those with normal lipid levels. Since high lipid often coincides with changes in hematocrit, adjusting hematocrit levels in the model can help better simulate the actual conditions. Currently, based on Eq. (4), three different values of H_D are adopted, i.e. $H_D = 0.45, 0.49$ and 0.53. Figure 3 shows the blood viscosity μ versus the diameter of blood vessels for different H_D. For most vessels in the retina, the vessel diameter is less than 200 μm. As shown in Fig. 3, it can be seen that the viscosity coefficient increases monotonically with the increase of H_D. The viscosity coefficient increases by approximately 10% when H_D is increased from 0.45 to 0.49, and it further increases by about 20% when H_D is increased to 0.53.

Figure 4 depicts the distributions of static pressure and velocity magnitude in the retinal vein network for different hematocrit, simulating the influence of elevated blood lipids. By comparing Figs. 4a, b and 1a, it can be observed that there is minimal variation in the velocity distribution as blood viscosity increases. This includes both the maximum velocity value and its position. This phenomenon can be easily understood since we maintain constant entrance velocities at all inlets and a fixed pressure at the outlet. As a result, an increase in viscosity does not directly result in a decrease in velocity. However, it does require a greater driving force throughout the flow within the venous tree, specifically an increased pressure difference. As shown in Fig. 4c, d, it is clear that the maximum pressure difference increases as viscosity increases. The pressure drop between the Inlet In6 and the outlet is approximately 10.8 mmHg for $H_D = 0.49$, which further increases to 11.9 mmHg for $H_D = 0.53$.

Figure 5 shows the distributions of WSS magnitudes in the retinal vein network, which were obtained by varying the hematocrit levels to simulate the impact of elevated blood lipids. By comparing it with Fig. 2a, we can clearly observe that as the viscosity coefficient increases, there is a consistent increase in WSS at all positions within the retinal veins. This overall increase amounts to approximately 10–20%. To provide more quantitative insights for comparison purposes, Table 1 presents detailed values of mean WSS magnitudes specifically for segments S14 and S22 under different hematocrit conditions (H_D). For instance, in segment S22, we observed an increment from 4.80 Pa to 5.79 Pa in mean WSS as H_D varied from 0.45 to 0.53. Furthermore, it is worth noting that this trend holds true across various segments within the retinal vein network. The relationship between mean WSS and viscosity μ exhibits an almost linear manner for representative segments such as S14 and S22.

The above findings contribute valuable insights into understanding how changes in lipid levels can influence hemodynamic parameters like pressure and WSS within retinal veins. Such knowledge could potentially aid in further investigations related to vascular health and disease progression associated with altered blood lipid profiles or other physiological factors affecting viscosity coefficients.

The potential effect of obstruction

The occurrence of retinal vein thrombosis might also be associated with hyperlipidemia, a condition that is characterized by elevated levels of lipids, particularly cholesterol and triglycerides, in the bloodstream. For instance, dyslipidemia was proven to be a risk factor for retinal vascular occlusion[21]. From a physiological

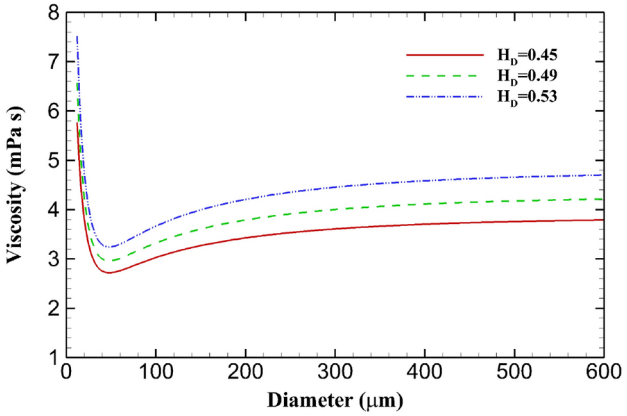

Fig. 3. The variation of viscosity μ versus diameter (D) of blood vessels for three values of H_D.

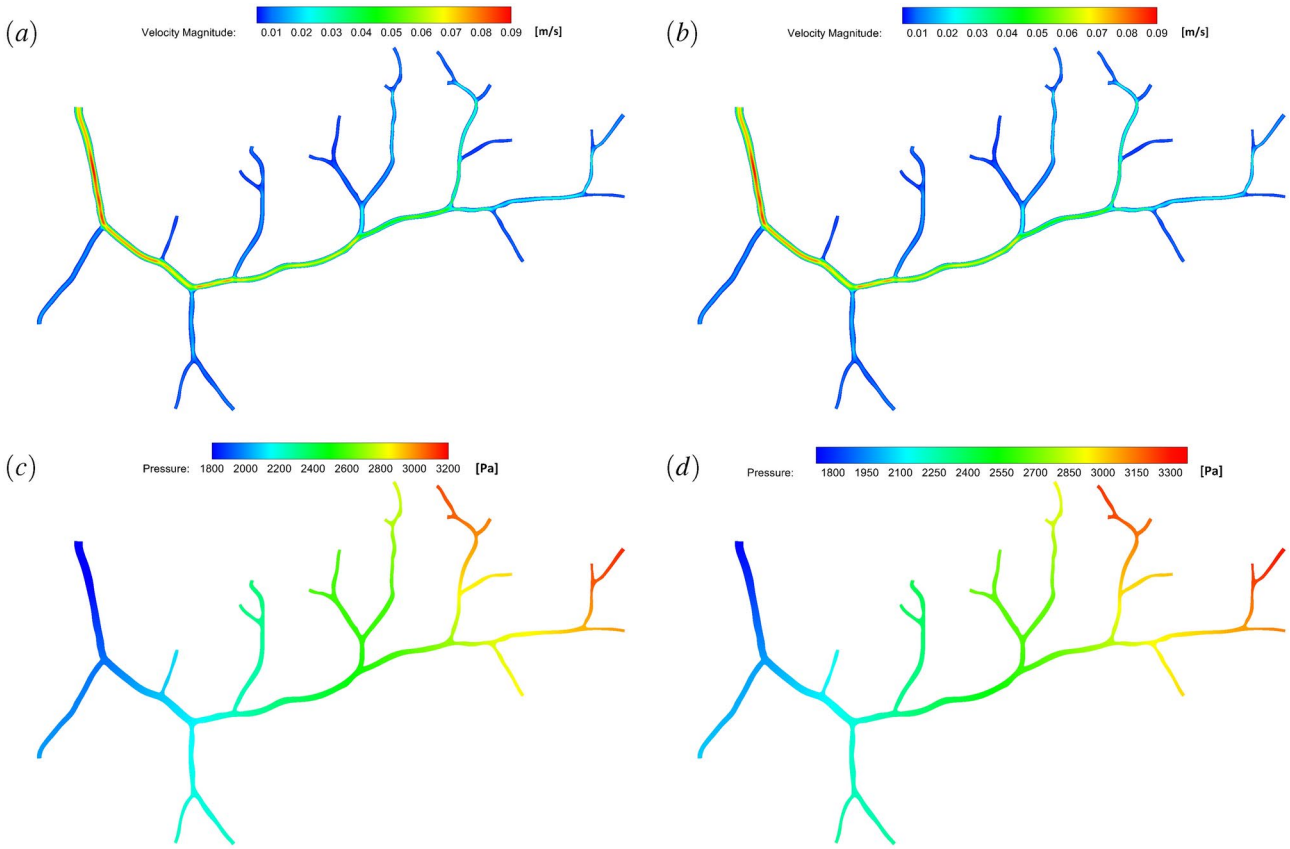

Fig. 4. The distributions of static pressure and velocity magnitude in retinal vein network for different hematocrit to mimic the influence of elevated blood lipids: velocity magnitude for (**a**) $H_D = 0.49$ and (**b**) $H_D = 0.53$; static pressure for (**c**) $H_D = 0.49$ and (**d**) $H_D = 0.53$.

standpoint, hyperlipidemia can significantly impact blood rheology, resulting in increased blood viscosity and an enhanced tendency for platelet aggregation. These physiological changes can create a conducive environment for thrombus formation, whereby blood clots develop within the venous system. Once formed, these thrombi can obstruct the retinal veins, impeding normal blood flow and leading to a range of complications. This vascular obstruction may result in various retinal pathologies, including retinal ischemia, macular edema, and even retinal hemorrhage. Such conditions can severely compromise visual function, potentially leading to substantial visual impairment or loss.

The present research focus has been on investigating the impact of thrombus-induced blockage within the venous vessel. In order to gain a comprehensive understanding of this phenomenon, we have specifically chosen segment S22 for our study. This particular branch vessel, as depicted in Figs. 2 and 5, has emerged as an area of utmost significance. Figure 6 illustrates different blockage cases of the S22 segment due to thrombosis in the venous tree. To further investigate the impact of thrombus-induced blockage in segment S22, we have simulated different cases using computational models. Figure 6 illustrates three distinct scenarios where varying degrees of blockage ratios are considered - Case B20, Case B40, and Case B60. In these simulations, a red-colored lump represents the simulated thrombi adhering to the inner lining of the blood vessel. The blockage ratio refers to the difference between 1 (representing an unobstructed vessel) and the ratio of the occluded vessel diameter to its original diameter. By considering different blockage ratios ranging from 20% to 60%, we can assess how varying levels of obstruction affect blood flow dynamics in segment S22.

In actual computations, the parameter H_D is selected to be 0.53, specifically considering the scenario where patients with vascular blockages often have high blood lipid levels. Figure 7 shows local distributions of velocity magnitudes with and without blockage around segment S22. The observation indicates that a highly conspicuous phenomenon is the significant enhancement of local blood flow speed caused by thrombus-induced blockages. The magnitude of the velocity in the center of the normal vessel is approximately 0.035 m/s, as depicted in Fig. 7a. With a mild level of obstruction in Case B40, there is an increase in velocity magnitude to 0.055 m/s near the lump. In Case B60 with severe obstruction, the peak velocity magnitude near the lump further increases to 0.086 m/s, as illustrated in Fig. 7d. Moreover, Fig. 7 reveals another prominent pattern, wherein the high-speed regions resulting from blockage are primarily concentrated around the lump, and the extent of this area increases proportionally with the size of the lump. Under the present configuration, the thrombus-induced local obstruction seems to have a minimal effect on the flow of surrounding blood vessels. For example, there have been minimal alterations in the velocity magnitude distributions in segments 21 and S29.

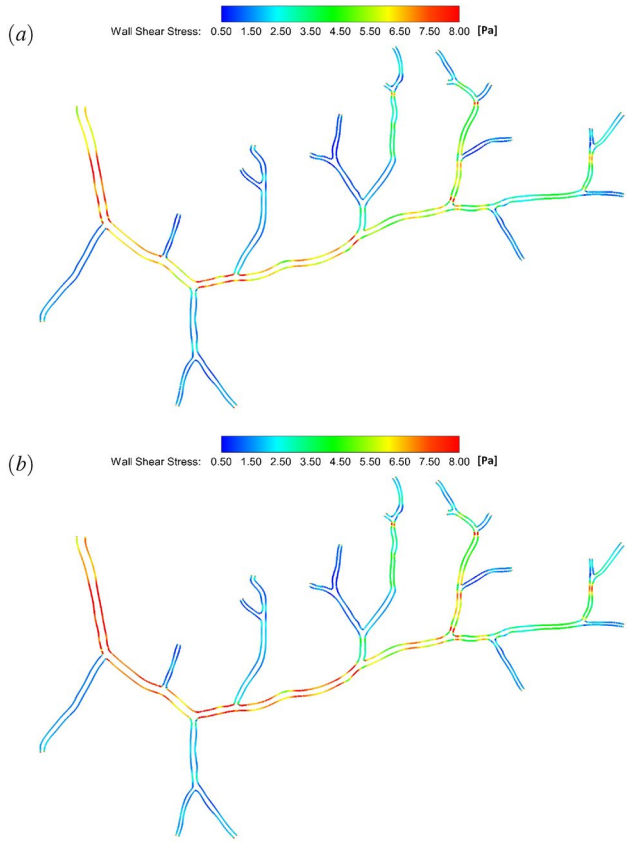

Fig. 5. The distributions of wall shear stress magnitudes in the retinal vein network for different hematocrit to mimic the influence of elevated blood lipids. (**a**) $H_D = 0.49$ and (**b**) $H_D = 0.53$.

Segment	Mean WSS ($H_D = 0.45$) (Pa)	Mean WSS ($H_D = 0.49$) (Pa)	Mean WSS ($H_D = 0.53$) (Pa)
S14	2.36	2.59	2.87
S22	4.80	5.26	5.79

Table 1. The magnitudes of mean wall shear stress in the S14 and S22 segments under different viscosity scenarios.

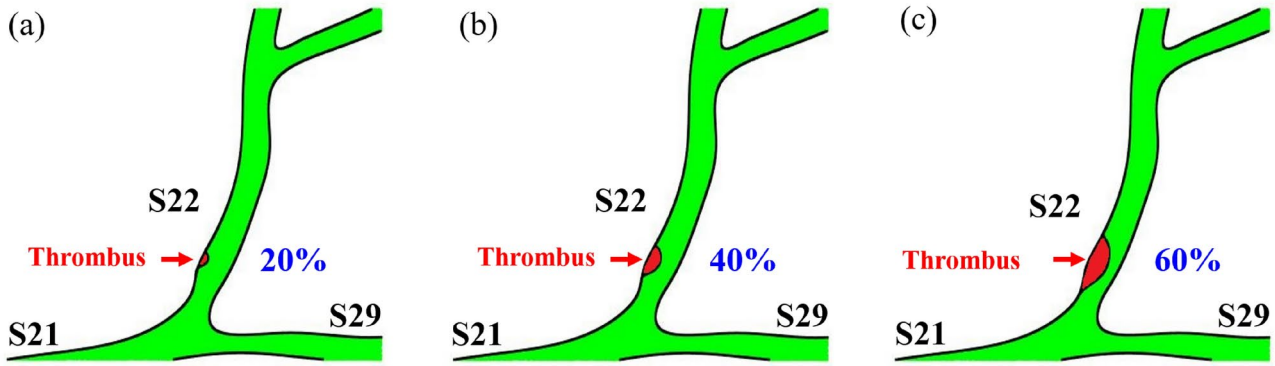

Fig. 6. Illustration of the blockage of the S22 segment due to thrombus formation in the venous tree. Three cases are modeled with different blockage ratios: (**a**) Case B20: blockage ratio 20%; (**b**) Case B40: blockage ratio 40%; (**c**) Case B60: blockage ratio 60%. The red-colored lump is utilized to mimic the thrombus, which adheres to the endothelial lining of the blood vessel.

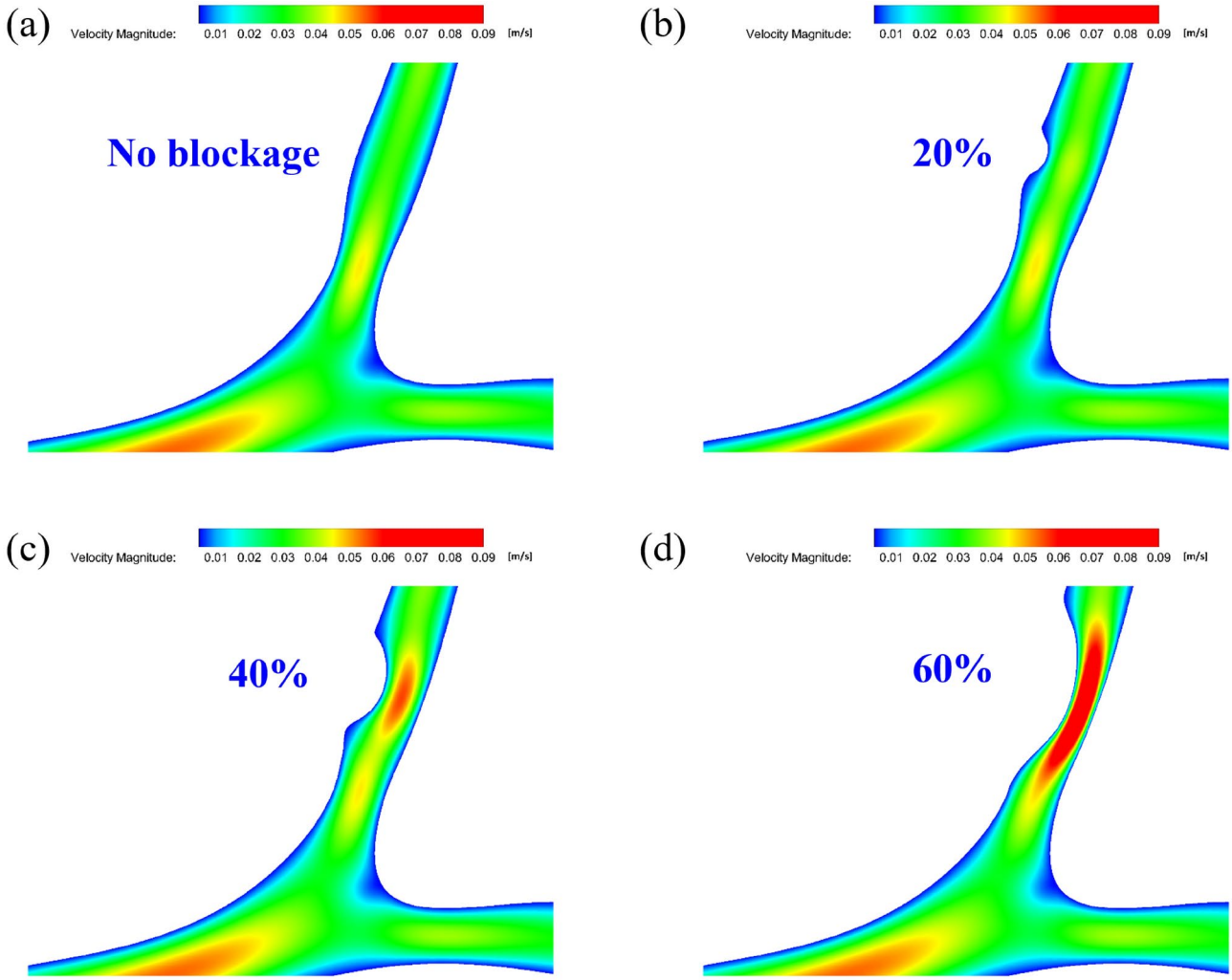

Fig. 7. Local distributions of velocity magnitudes with and without blockage around segment S22. (**a**) No blockage; (**b**) Case B20: blockage ratio 20%; (**c**) Case B40: blockage ratio 40%; (**d**) Case B60: blockage ratio 60%.

Figure 8 shows local distributions of WSS magnitudes with and without blockage in the vicinity of the lump in segment S22. The magnitude of WSS around the lump exhibits a significant increase with an increasing blockage ratio, similar to the velocity distribution. In all cases with blockage, the apex of the lump is where the maximum WSS usually occurs. As depicted in Fig. 8a, for a normal vessel, the peak magnitude of WSS is approximately 5 Pa. However, this value significantly rises to around 16 Pa in Case B40 and 33 Pa in Case B60, as shown in Fig. 8c, d. Another significant feature is that there are very small WSS at the ends of the lump, which means that the rate of change of WSS in this area is very large. This long-term local high shear force around the lump may cause serious consequences, including endothelial dysfunction, which could compromise the integrity of the blood-retina barrier and increase the risk of ischemia and vascular damage. Additionally, consistent exposure to extremely high shear stress levels can result in morphological changes in the retinal vessels, potentially contributing to the pathogenesis of various ocular diseases. Furthermore, a noteworthy finding is that the local obstruction in segment S22 would have minimal impact on the distribution of WSS in adjacent vessel segments, which is consistent with the velocity distribution.

Discussion

The present study utilizes CFD to investigate the impact of elevated blood lipids on hemodynamics within the human retinal vasculature. Our findings provide valuable insights into the interplay between blood rheology and retinal vascular health, contributing to the understanding of retinal vein occlusion or other vascular complications.

Our computational analysis revealed that the average flow velocity in arterial vessels is higher than in venous vessels, which aligns with the established understanding of retinal hemodynamics where arterial flow is typically faster due to lower resistance in arterioles. The observation is that venous vessels experience more pronounced WSS since venous vessels are often more tortuous and have more branches, leading to higher WSS. A significant

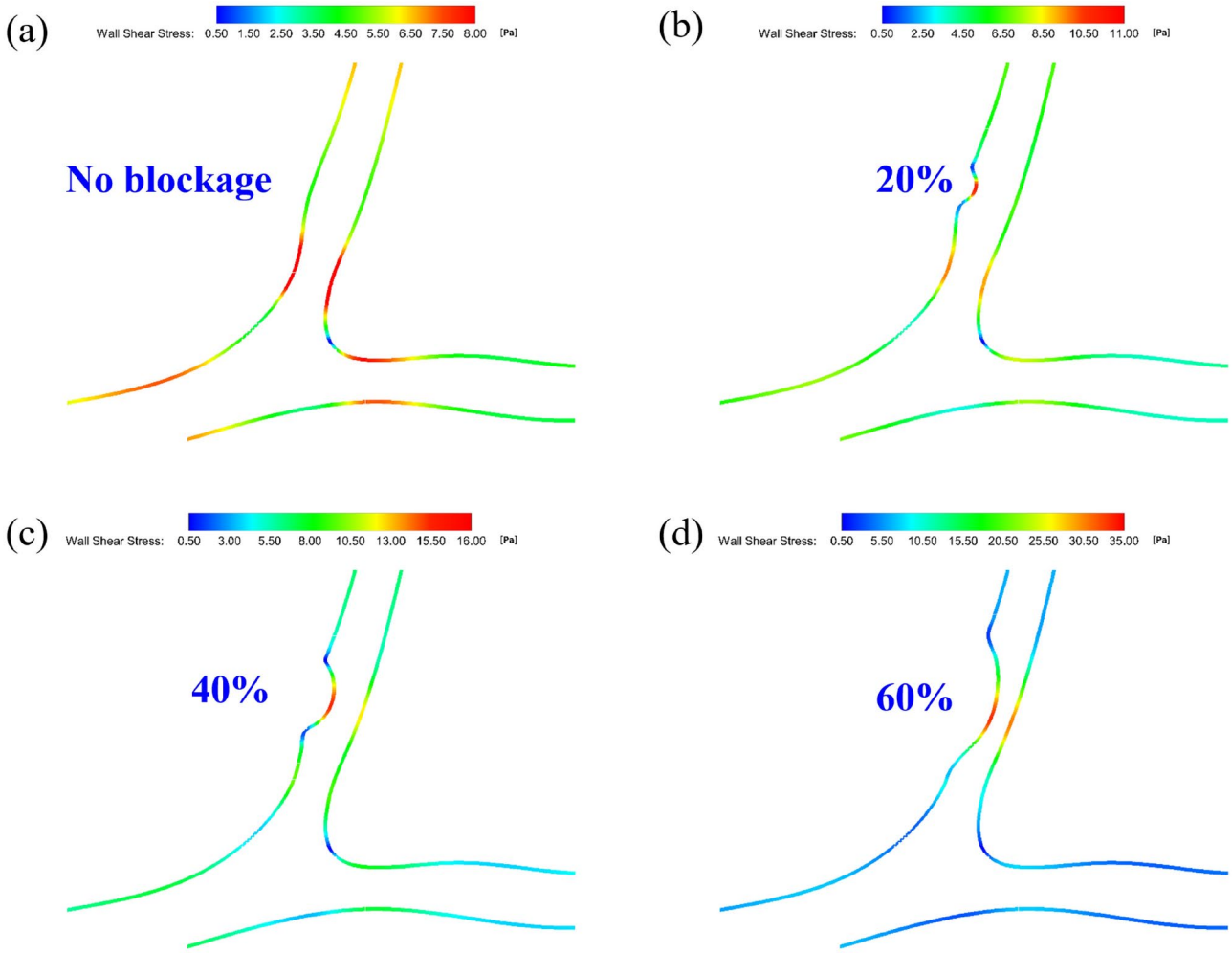

Fig. 8. Local distributions of wall shear stress magnitudes with and without blockage around segment S22 in the vicinity of the lump. (**a**) No blockage; (**b**) Case B20: blockage ratio 20%; (**c**) Case B40: blockage ratio 40%; (**d**) Case B60: blockage ratio 60%.

result from our simulations is the increased WSS in vessels with more branches, particularly in the venous network. This finding underscores the importance of considering vascular architecture when assessing the risk of retinal vascular diseases, as areas of significant changes in WSS are known to be associated with endothelial dysfunction. The simulation of elevated blood lipids by increasing viscosity in venous vessels by approximately 10-20% resulted in a corresponding increase in WSS. This result is particularly relevant as it suggests that hyperlipidemia could exacerbate the risk of vascular damage through increased WSS, which could potentially lead to vascular complications. The near-linear relationship between mean WSS and viscosity observed in our study indicates a direct and predictable effect of blood lipid levels on hemodynamic parameters. Furthermore, our investigation into the potential blockage caused by increased blood lipids, through the simulation of thrombus formation in critical branches, revealed a significant increase in local blood flow speed and WSS. This finding is concerning as it indicates that even moderate obstructions can lead to substantial changes in local hemodynamics, potentially contributing to the pathogenesis of ocular diseases.

It is important to acknowledge the limitations of this study. The assumptions of steady blood flow and rigid vessel walls may not fully capture the dynamic nature of blood flow and vessel compliance in vivo. Additionally, the simulation of blood as a non-Newtonian fluid with variable viscosity based on hematocrit and vessel diameter may not account for all the complexities of blood rheology, such as the effects of red blood cell aggregation and plasma protein interactions. Despite these limitations, our study offers a comprehensive computational analysis, revealing some clear variation trends due to increased lipid levels. These trends are likely to remain valid and can therefore potentially inform future research and clinical practice. The findings highlight the need for further investigation into the role of systemic health parameters, such as blood lipid levels, in the development and progression of retinal vascular diseases. Moreover, our results emphasize the potential utility of CFD in predicting and preventing hyperlipidemia-associated retinal diseases, suggesting that interventions targeting blood lipid levels could be crucial in maintaining retinal vascular health and preventing vision loss.

In conclusion, this study provides a computational framework to assess the influence of blood lipids on retinal hemodynamics, contributing to the growing body of research at the intersection of ocular medicine

and computational modeling. The results suggest that elevated blood lipids could significantly impact retinal vascular health through alterations in blood viscosity and the potential for thrombus-induced obstructions. These findings warrant further exploration and could have important implications for preventing and treating retinal vascular diseases. Additionally, in the future, retinal pathology circulations deserve to be investigated in detail with more samples if subject-specific flow measurements are available.

Methods

This study was approved by the Institutional Review Board of the First People's Hospital of Hefei (2024-237-02) by following all human subject investigation guidelines and adhering to tenets of the Declaration of Helsinki.

Figure 9 shows the retinal image with a resolution of 1536 $\times$ 1536 pixels, which has been obtained from a healthy female adult by a Heidelberg spectralis HRA+OCT - 55° Field of View. The field view in this image is corresponding to a physical domain with a size of 1.72 cm (wide)$\times$ 1.72 cm (height). To facilitate the analysis of these vessels, the image was first processed using the software 3D Slicer version 5.6.2. to enhance contrast, which is a free, open-source software for visualization, processing, segmentation, registration, and analysis of medical, biomedical, and other 3D images. Then, the image was further processed in Matlab to determine the boundaries of these vessels. and the accuracy of the model was maintained within a tolerance of less than 1 pixel ($\sim 11\mu$ m) through meticulous control of the geometric description. The boundary information is utilized in PointWise software for model construction and mesh generation. In this study, the focus was narrowed to the subtemporal branch vessels of the retina, specifically the artery and vein trees that are highlighted in red and blue, respectively. These were selected for a two-dimensional (2D) computational analysis. To ensure the accuracy of the numerical computations, the finer vessels were intentionally excluded from the analysis. Currently, the diameters of vessels shown in Fig. 9b range from about 47 to 204 μm. The accuracy of the model is satisfactory for the majority of arterial and venous branches, with the exception of some smallest bifurcated vessels. However, it should be noted that addressing this issue is not feasible at present, as it would require more advanced OCT equipment that may be developed in the future. Figure 10 shows the simplified outline of the image-based retinal vein and artery vessel networks under healthy conditions. The venous network is characterized by 18 inlets, and a single outlet, and consists of 35 segments, each labeled as Si where i ranges from 1 to 35. Conversely, the arterial network is comprised of a single inlet and 18 outlets, each denoted as Oi with i also ranging from 1 to 18, and includes 35 segments.

For simulating the blood flow in the retina, the incompressible Navier-Stokes equations have been solved, which have the form of

$$\frac{\partial \mathrm{u}}{\partial t} + \mathrm{u} \cdot \nabla \mathrm{u} = -\frac{1}{\rho}\nabla p + \nu \nabla^2 \mathrm{u}, \tag{2}$$

$$\nabla \cdot \mathrm{u} = 0, \tag{3}$$

where u is the velocity vector, and ρ is the blood density. The dynamic viscosity, represented by $\nu = \mu/\rho$, refers to the measure of a fluid's resistance to flow, where μ represents the kinematic viscosity. In this study, the blood

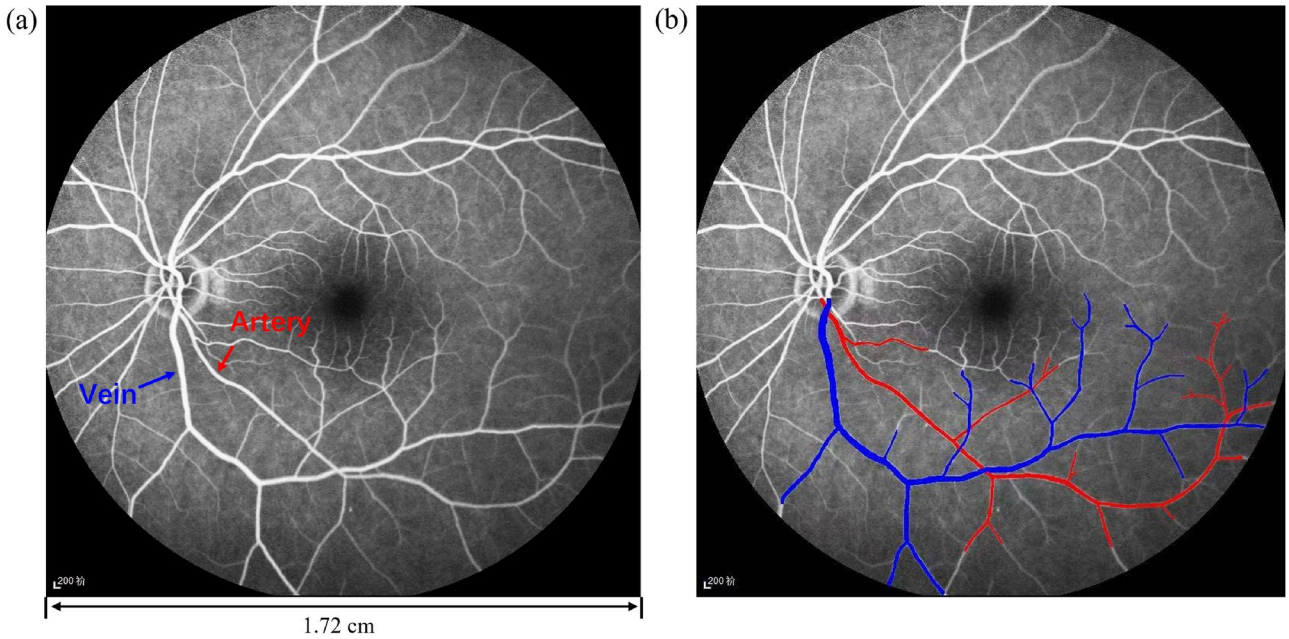

Fig. 9. (**a**) Illustration of the pre-processing treatment for original image for a healthy adult. (**b**) The marked-red artery tree and the marked-blue vein tree are examined in this study..

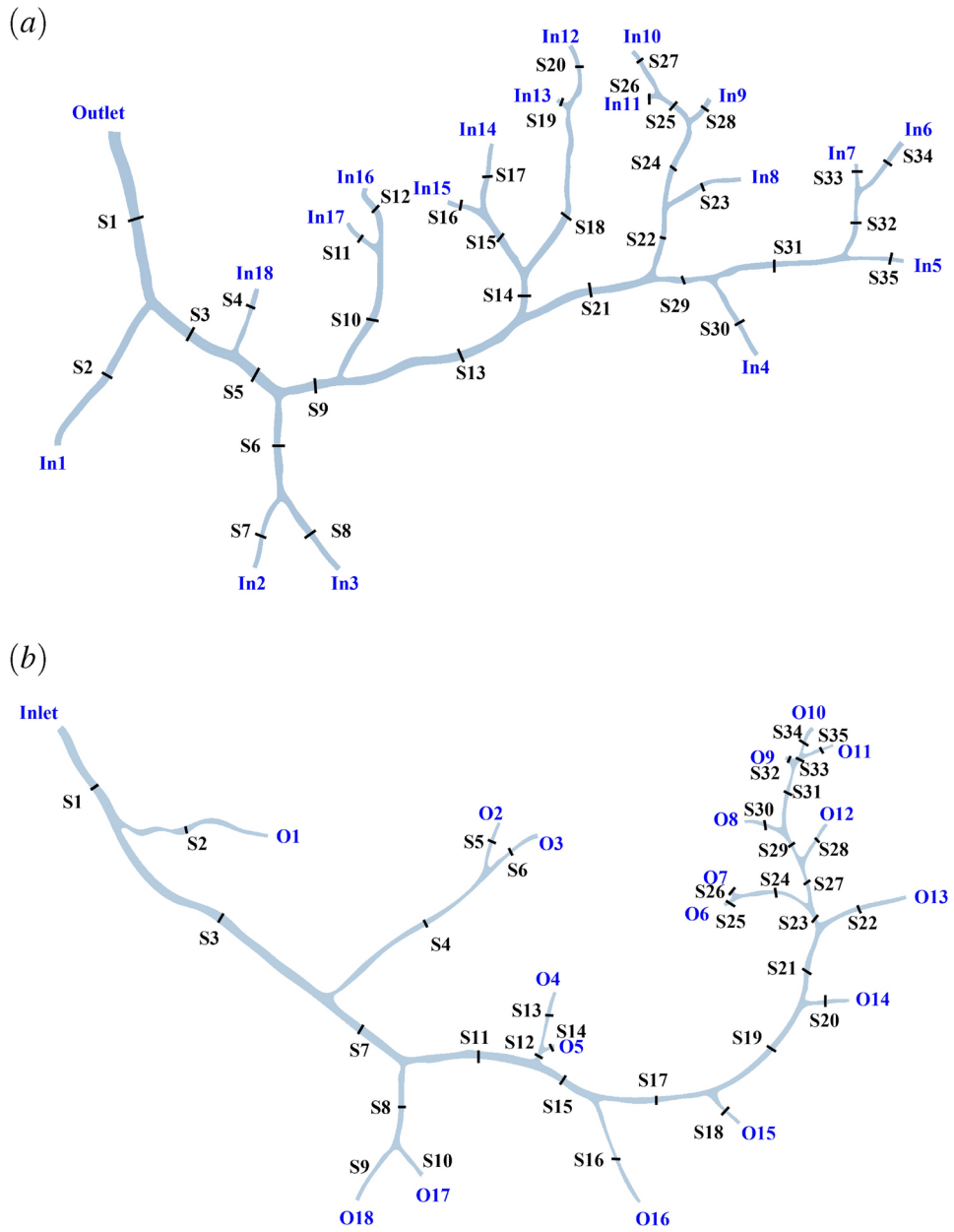

Fig. 10. Simplified outline of the image-based (**a**) retinal venous tree and (**b**) retinal arterial tree. The inlet (In1 to In18) and outlet (O1 to O20) are shown.

flow is assumed to be steady in time, and the blood vessels are assumed to be rigid. Also, the blood is assumed to be a non-Newtonian fluid consisting of plasma and blood cells. The blood density is $1055\ \mathrm{kg/m}^3$[11], which is kept constant throughout the study. To simulate the microcirculation involving vessel diameters below 500 μm, the Fahraeus-Lindqvist (FL) model[22] is utilized for hemodynamical simulations. The viscosity is assumed to be a function of diameter and hematocrit (H_D). In this study, the expression of viscosity is given by[23]

$$\mu_{rel}(D, H_D) = \frac{\mu}{\mu_{plasma}} = \left[1 + (\mu_{0.45} - 1) \cdot \frac{(1 - H_D)^C - 1}{(1 - 0.45)^C - 1} \cdot \left(\frac{D}{D - 1.1}\right)^2\right] \cdot \left(\frac{D}{D - 1.1}\right)^2 \quad (4)$$

where μ_{plasma} represents the dynamic viscosity of the plasma, and $\mu_{plasma} = 1.2$ mPa s[24] is adopted for a healthy person. Normally, $\mu_{0.45}$ denotes the blood viscosity for a fixed hematocrit, i.e., $H_D = 0.45$:

$$\mu_{0.45} = 6\mathrm{e}^{-0.085D} + 3.2 - 2.44\mathrm{e}^{-0.06D^{0.545}} \quad (5)$$

where D is the diameter of the vessel, and the power parameter C that describes the shape of viscosity dependence[23] is expressed as

$$C = \left(0.8 + e^{-0.0750}\right) \cdot \left(-1 + \frac{1}{1 + 10^{-11} \cdot D^{12}}\right) + \frac{1}{1 + 10^{-11} \cdot D^{12}}. \quad (6)$$

It is worth mentioning that the parameter H_D has been adjusted to account for the possible impact of blood lipids.

The governing equations are solved using a finite-volume flow solver (Ansys Fluent). A laminar flow regime is used for each case and no turbulence model is utilized since Reynolds numbers are below 20 in this study. For the discretization of the momentum equation, a second-order upwind scheme is employed for the convective terms, and the second-order central scheme is used for the viscous terms. Pressure-velocity coupling in mass and momentum equations is solved using the semi-implicit method for pressure-linked equations (SIMPLE) algorithm. Implicit iteration is adopted for the steady flow simulation, and the convergence criteria are set to 10^{-4}. The specification of boundary conditions is essential for obtaining accurate results. For both artery and vein vessels, the no-slip boundary conditions have been imposed on the endothelial surface of the blood vessel. Similar to previous studies[11], the clinical measurement data reported from the literature will be imposed on the inflow and outflow boundaries to mimic the realistic inlet and outlet boundary conditions. In certain applications involving large blood vessels[25,26], it has been observed that tissue degradation has been associated with both changes in WSS and oscillatory shear index (OSI). However, according to the pulsatile simulations for retinal hemodynamics conducted by Rebhan et al.[12], it was found that the transient flow was virtually absent, and the OSI in all pulsatile cases was practically zero, indicating unidirectional shear stress. Their results implies that a pulsatile waveform may not be necessary for the flow in the retinal microvessels. In the case of arteries, a Dirichlet boundary condition has been imposed at the inlet with a constant value of 7.3 cm/s[11], since the mean blood velocity in the Central Retinal Artery (CRA) was reported as 7.35 ± 2.7 cm/s in vivo measurements[17]. Murray's law and mean flow conditions are used to evaluate the vascular resistance at each outlet, following the strategies of previous studies[11–13]. In the case of veins, the inlet velocities have been set in the range of 5.6 mm/s to 9.7 mm/s, according to their diameters. Previous studies have shown that the venous velocity has ranged approximately from 5 to 25 mm/s with a diameter between 60 and 180 μm[27,28]. The velocity increases in a nearly linear manner as the diameter increases. The outlet has been set to maintain a pressure of 13 mmHg refer to Malek et al.[11], as the noninvasive measurements indicate a Central Retinal Vein Pressure (CRVP) value of 15.0 ± 2.7 mmHg[29].

Figure 11 demonstrates the meshing strategy used for the vein vessels in this study. The unstructured mesh with quad and triangle elements is employed, while the quad elements are clustered near the boundary, and the triangle elements are filled in the middle region. This strategy can ensure the accuracy of the velocity gradient near the wall, which directly influences the computation of WSS. In this study, a fine mesh comprising a total number of 1,846,405 cells is utilized for the retinal vein, whereas a mesh with 674,238 cells is employed for the artery. For validating the CFD simulation, we performed a mesh independence study and refined it with a total cell number of 3,737,206. Table 2 presents the detailed mesh specifications for both the initial vein mesh employed in this study and its refined counterpart. Figure 12 illustrates the velocity profiles at the outlet of the retinal vein. It is evident that the velocities computed using the refined mesh are consistent with those obtained from the present vein mesh, suggesting that the numerical solution has achieved convergence. It should be emphasized that accurate verification remains a formidable challenge at present, since that we did not have

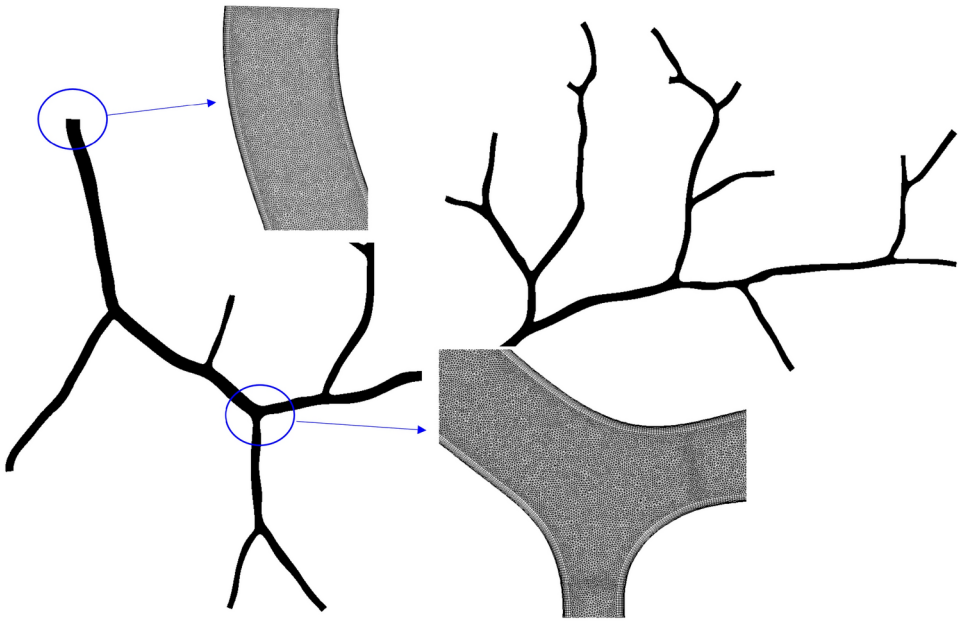

Fig. 11. The meshing strategy used for the vein vessels in this study: the Quads cells are used and clustered near the vessel surface and the Triangles elements are used in the middle region..

Mesh details	Present vein mesh	Refined vein mesh	Present artery mesh
Triangles	1,360,100	2,835,734	458,708
Quads	486,305	901,472	215,530
Total Cells	1,846,405	3,737,206	674,238

Table 2. The details for both the vein and artery meshes utilized in the present study and the refined vein mesh.

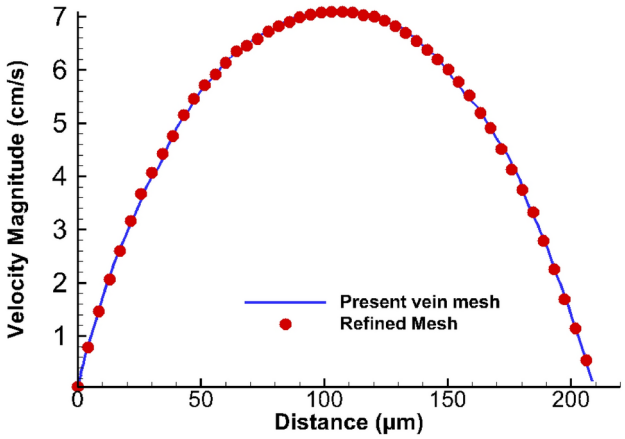

Fig. 12. The velocity profiles at the outlet for the retinal vein: the results are computed using the present vein mesh and the refined mesh, respectively.

Methods	CRV velocity (cm/s)	CRV velocity (cm/s)	PDRA (mmHg)
Mendfvil[17] (in vivo measurement)	12.6 ± 2.6	4.42 ± 0.51	–
Çaça[18] (in vivo measurement)	11.25 ± 2.38	3.96 ± 1.34	–
Liu[19] (prediction)	11.5	–	11–14.6
Malek[11] (prediction)	11	5.4	11–13
Present (prediction)	11	5.6	11

Table 3. Comparison of velocity and pressure drop between the present study and in vivo measurements/ numerical predictions reported in the literature. *CRA* central retinal artery, *CRV* central retinal vein, *PDRV* pressure drop for the retinal artery.

subject-specific flow measurements. Here, for validation purposes, Table 3 presents a comparative analysis of the velocity and pressure drop data obtained from the current study alongside in vivo measurements reported in the literature. Generally, the present simulation results show reasonable agreement with the experimental measurements and prior predictions, despite some deviations still being observed between different studies, which can be attributed to variations in models and specified inlet/outlet conditions. It should be emphasized that subject-specific flow measurements, such as the pressure and velocities at the inlet and outlet, are scarce at present, which significantly restricts the comprehensive investigation of hemodynamics within human retinal vessels.

Data availability

The datasets generated and/or analysed during the current study are available from the corresponding author on reasonable request.

Received: 23 November 2024; Accepted: 14 April 2025
Published online: 13 May 2025

References

1. Fitzpatrick, M. J. & Kerschensteiner, D. Homeostatic plasticity in the retina. *Prog. Retin. Eye Res.* **94**, 101131. https://doi.org/10.1016/j.preteyeres.2022.101131 (2023).
2. Siggers, J. H. & Ethier, C. R. Fluid mechanics of the eye. *Annu. Rev. Fluid Mech.* **44**, 347–372 (2012).

3. Hickam, J. B. & Frayser, R. Studies of the retinal circulation in man: Observations on vessel diameter, arteriovenous oxygen difference, and mean circulation time. *Circulation* **33**, 302–316. https://doi.org/10.1161/01.CIR.33.2.302 (1966).
4. Ghanchi, F. The royal college of ophthalmologists' clinical guidelines for diabetic retinopathy: A summary. *Eye* **27**, 285–287 (2013).
5. Khayat, M., Williams, M. & Lois, N. Ischemic retinal vein occlusion: Characterizing the more severe spectrum of retinal vein occlusion. *Surv. Ophthalmol.* **63**, 816–850. https://doi.org/10.1016/j.survophthal.2018.04.005 (2018).
6. The Complications of Age-Related Macular Degeneration Prevention Trial Study Group. The Complications of Age-Related Macular Degeneration Prevention Trial (CAPT): Rationale, design and methodology. *Clinical Trials* **1**, 91–107. https://doi.org/10.1191/1740774504cn007xx (2004).
7. Lee, C.-Y.J., Kim, K.-C., Park, H.-W., Song, J.-H. & Lee, C.-H. Rheological properties of erythrocytes from male hypercholesterolemia. *Microvasc. Res.* **67**, 133–138. https://doi.org/10.1016/j.mvr.2003.12.006 (2004).
8. Wu, D. et al. Retinal ischemia-reperfusion injury induces intense lipid synthesis and remodeling. *Biochem. Biophys. Res. Commun.* **689**, 149232. https://doi.org/10.1016/j.bbrc.2023.149232 (2023).
9. Triviño, A. et al. Effects of hypercholesterolaemia in the retina. In *Ocular Diseases*. https://doi.org/10.5772/48359 (IntechOpen) (2012).
10. Ganesan, P., He, S. & Xu, H. Analysis of retinal circulation using an image-based network model of retinal vasculature. *Microvasc. Res.* **80**, 99–109. https://doi.org/10.1016/j.mvr.2010.02.005 (2010).
11. Malek, J. et al. Computational analysis of blood flow in the retinal arteries and veins using fundus image. *Comput. Math. Appl.* **69**, 101–116. https://doi.org/10.1016/j.camwa.2014.11.017 (2015).
12. Rebhan, J., Parker, L. P., Kelsey, L. J., Chen, F. K. & Doyle, B. J. A computational framework to investigate retinal haemodynamics and tissue stress. *Biomech. Model. Mechanobiol.* **18**, 1745–1757. https://doi.org/10.1007/s10237-019-01172-y (2019).
13. Tripathy, K. C., Siddharth, A. & Bhandari, A. Image-based insilico investigation of hemodynamics and biomechanics in healthy and diabetic human retinas. *Microvasc. Res.* **150**, 104594. https://doi.org/10.1016/j.mvr.2023.104594 (2023).
14. Kamada, H., Nakamura, M., Ota, H., Higuchi, S. & Takase, K. Blood flow analysis with computational fluid dynamics and 4D-flow MRI for vascular diseases. *J. Cardiol.* **80**, 386–396. https://doi.org/10.1016/j.jjcc.2022.05.007 (2022).
15. Wang, H., Krüger, T. & Varnik, F. Effects of size and elasticity on the relation between flow velocity and wall shear stress in side-wall aneurysms: A lattice Boltzmann-based computer simulation study. *PLOS ONE* **15**, e0227770. https://doi.org/10.1371/journal.pone.0227770 (2020).
16. Wang, H., Fan, L., Choy, J. S., Kassab, G. S. & Lee, L. C. Simulation of coronary capillary transit time based on full vascular model of the heart. *Comput. Methods Prog. Biomed.* **243**, 107908. https://doi.org/10.1016/j.cmpb.2023.107908 (2024).
17. Mendivil, A., Cuartero, V. & Mendivil, M. P. Ocular blood flow velocities in patients with proliferative diabetic retinopathy and healthy volunteers: A prospective study. *Br. J. Ophthalmol.* **79**, 413–416. https://doi.org/10.1136/bjo.79.5.413 (1995).
18. ÇaÇa, İ et al. Color doppler imaging of ocular hemodynamic changes in Behçet's disease. *Jpn. J. Ophthalmol.* **48**, 101–105 (2004).
19. Liu, D. et al. Computational analysis of oxygen transport in the retinal arterial network. *Curr. Eye Res.* **34**, 945–956 (2009).
20. Zhou, M. et al. Wall shear stress and its role in atherosclerosis. *Front. Cardiovasc. Med.* **10**, 1083547 (2023).
21. Zheng, C. et al. Plasma lipid levels and risk of retinal vascular occlusion: A genetic study using Mendelian randomization. *Front. Endocrinol.* **13**, 954453. https://doi.org/10.3389/fendo.2022.954453 (2022).
22. Fahraeus, R. & Lindqvist, T. The viscosity of the blood in narrow capillary tubes. *Am. J. Physiol.-Legacy Content* **96**, 562–568 (1931).
23. Pries, A., Secomb, T. W. & Gaehtgens, P. Biophysical aspects of blood flow in the microvasculature. *Cardiovasc. Res.* **32**, 654–667 (1996).
24. Fung, Y.-C. *Biomechanics: Mechanical Properties of Living Tissues* (Springer, 2013).
25. Wang, H., Balzani, D., Vedula, V., Uhlmann, K. & Varnik, F. On the potential self-amplification of aneurysms due to tissue degradation and blood flow revealed from FSI simulations. *Front. Physiol.* **12**, 785780. https://doi.org/10.3389/fphys.2021.785780 (2021).
26. Wang, H., Uhlmann, K., Vedula, V., Balzani, D. & Varnik, F. Fluid-structure interaction simulation of tissue degradation and its effects on intra-aneurysm hemodynamics. *Biomech. Model. Mechanobiol.* **21**, 671–683. https://doi.org/10.1007/s10237-022-01556-7 (2022).
27. Riva, C. E., Grunwald, J. E., Sinclair, S. H. & Petrig, B. Blood velocity and volumetric flow rate in human retinal vessels. *Invest. Ophthalmol. Vis. Sci.* **26**, 1124–1132 (1985).
28. Grunwald, J. E., Riva, C. E., Baine, J. & Brucker, A. J. Total retinal volumetric blood flow rate in diabetic patients with poor glycemic control. *Invest. Ophthalmol. Vis. Sci.* **33**, 356–363 (1992).
29. Stodtmeister, R. et al. Enhanced pressure in the central retinal vein decreases the perfusion pressure in the prelaminar region of the optic nerve head. *Invest. Ophthalmol. Vis. Sci.* **54**, 4698–4704 (2013).

Acknowledgements

The work is supported by the National Natural Science Foundation of China under Grant numbers of 82171043 and 82471094.

Author contributions

Y.D. designed the study plan, performed the relevant numerical analysis and drafted the manuscript. Z.J., J.J., G.Y. and Y.L. participated in analysing results. L.T. helped to conceive the study and modify the manuscript. All authors have read and approved the final manuscript.

Declarations

Competing interests

The authors declare no competing interests.

Additional information

Correspondence and requests for materials should be addressed to L.T.

Reprints and permissions information is available at www.nature.com/reprints.

Publisher's note Springer Nature remains neutral with regard to jurisdictional claims in published maps and institutional affiliations.